

Journal of Materials Chemistry C

Materials for optical, magnetic and electronic devices

Accepted Manuscript

This article can be cited before page numbers have been issued, to do this please use: R. Mulholland, T. Loan, J. O'Neill, J. Ghosh, S. Al-Ghamdi, S. Hinder, A. Longcake, M. Probert, H. Salway, M. Anaya, P. Sellin and C. Crean, *J. Mater. Chem. C*, 2026, DOI: 10.1039/D5TC03935E.



This is an Accepted Manuscript, which has been through the Royal Society of Chemistry peer review process and has been accepted for publication.

Accepted Manuscripts are published online shortly after acceptance, before technical editing, formatting and proof reading. Using this free service, authors can make their results available to the community, in citable form, before we publish the edited article. We will replace this Accepted Manuscript with the edited and formatted Advance Article as soon as it is available.

You can find more information about Accepted Manuscripts in the [Information for Authors](#).

Please note that technical editing may introduce minor changes to the text and/or graphics, which may alter content. The journal's standard [Terms & Conditions](#) and the [Ethical guidelines](#) still apply. In no event shall the Royal Society of Chemistry be held responsible for any errors or omissions in this Accepted Manuscript or any consequences arising from the use of any information it contains.

1D All-Inorganic Metal Halide Rb_2AgX_3 ($\text{X} = \text{Cl}, \text{Br}$): Pb-Free Scintillator Materials for Ionising Radiation Detection

View Article Online
DOI: 10.1039/D5TC03935E

Roma Mulholland,¹ Tommy Loan,² Joseph O'Neill,³ Joydip Ghosh,³ Suad Al-Ghamdi,³ Steven Hinder,⁴ Alexandra Longcake⁵, Michael R. Probert⁵, Hayden Salway,⁶ Miguel Anaya,⁶ Paul Sellin,³ Carol Crean^{1*}

¹*School of Chemistry and Chemical Engineering, University of Surrey, Guildford, UK*

²*Edinburgh Instruments, 2 Bain Square, Livingston Village, Livingston, UK*

³*School of Mathematics and Physics, University of Surrey, Guildford, UK*

⁴*School of Mechanical Engineering Sciences, University of Surrey, Guildford, UK*

⁵*School of Natural and Environmental Sciences, Newcastle University, Newcastle upon Tyne NE1 7RU, UK*

⁶*Department of Chemical Engineering and Biotechnology, University of Cambridge, Cambridge, CB3 0AS UK*

Abstract

Rb-based metal halide materials possess large attenuation coefficients and bright luminescence making them suitable as scintillators for X-ray detection. Here, we present the first report of an optimised anti-solvent synthesis method enabling gram-scale preparation of phase-pure Rb_2AgX_3 , ($\text{X} = \text{Cl}, \text{Br}$) metal halides, which show broadband emission centred at 585 nm and 514 nm, respectively. We have identified solvent selection criteria that are broadly applicable to the synthesis of a wider variety of perovskite materials. This approach offers several advantages: reduced reaction temperatures, shorter reaction times, enhanced purity, and increased yields. Collectively, these improvements contribute to a more sustainable and scalable synthesis route.

Rb_2AgX_3 , ($\text{X} = \text{Cl}, \text{Br}$) metal halides report fast radiative recombination with typical decay times of sub-10 ns. Optical and radioluminescence measurements revealed halide-specific emission pathways with Rb_2AgCl_3 displaying superior emission intensities, whereas Rb_2AgBr_3 consistently elicited a stronger X-ray induced response. High pressure XRD studies measured bulk crystal moduli indicating that the Rb_2AgCl_3 crystal structure has a stiffer lattice than the Rb_2AgBr_3 analogue. Compressing pellets of polycrystalline Rb_2AgX_3 over a range of pressures (both at room temperature and 70 °C) confirmed this lattice stiffness trend and allowed for improvements in material densification and optical clarity at thicknesses of > 250 μm . The X-ray response of these pellets improved with increasing pressure for the bromide analogue underscoring the importance of microstructural control in enhancing scintillation efficiencies.



Introduction

View Article Online
DOI: 10.1039/D5TC03935E

Ionising radiation detection serves a broad range of applications that are critical to many areas of modern-day life; for characterisation and diagnostics in research and medical settings to security and nuclear energy monitoring in industry.ⁱ High energy X-ray photons can be indirectly detected based on the scintillation mechanism whereby incident X-rays are converted into lower energy UV/Vis photons that are measured at a photodetector. Current commercial scintillator options such as CsI:TI, (Lu,Y)₂SiO₅ (LYSO), Bi₄Ge₃O₁₂ (BGO) offer high light yields and energy resolutions however, high operating costs, rare and toxic material dependency as well as non-tuneable scintillation limit their potential.ⁱⁱ

The high atomic number of lead and the ease with which their emission can be tuned, has led to much research into the family of lead halide perovskites as candidates for scintillators and X-ray imagers.ⁱⁱⁱ These ABX₃ cubic materials have multiple points for substitution, which allows for great choice when designing the structure of perovskite scintillators. Both inorganic and organic A site options are available, in addition to tailoring the halide component, which gives an array of materials with a wide range of optical properties.^{iv}

The issue of Pb ion toxicity has driven research into replacement of the B-site cation with other ions including Sn, Ge, Cu, Ag, Na, Sb, In and Bi. A huge variety of structures can result, depending on the valency of the substituted ions, allowing for either homovalent or heterovalent exchanges to be made.⁴ Tailoring the ions in perovskites leads to a change in the crystal structure from the initial cubic materials studied. The nature of the substitution can lead to a change from the original 3D cubic structures, to 2D, 1D and even 0D analogues. This wide variety in both crystal and material structure alters both the electrical and optical properties accordingly.^v

Low-dimensional metal halide (LDMH) perovskites and their derivatives can be differentiated as either morphological or molecular. Reducing the dimensionality morphologically refers to quantum confinement in at least one direction but the material maintains the 3D crystal structure e.g. CsPbBr₃ 0D quantum dots, 1D nanowires or 2D nanoplatelets.^{vi} The intrinsic properties remain, only affected by the role of quantum confinement. On the molecular level, it is a standalone material that is defined by the spatial arrangement of the metal halide polyhedral along octahedral axes. Their dimensionality decreases through isolation of polyhedra across crystallographic planes. This equates to very different intrinsic properties, affecting band structures and electronic transport.^{vii} Lowering the dimensionality at the molecular level results in a deviation of the 'true' perovskite ABX₃ structure thus, they can no longer be referred to as perovskites and instead the term 'metal halide' is coined.



One-dimensional metal halides have drawn considerable attention for their unique luminescent properties. The metal halide polyhedra are connected along one direction as the A-site is occupied by in/organic cations resulting in a chain-like structure. Due to the quantum and dielectric confinement in two directions, both the bandgap and exciton binding energy increase considerably. One of the most notable features of these LDMHs are their broadband emission and large Stokes shift.⁵ Combining the promising optical properties, high RL intensity at ambient temperature and Pb-alterative options at the B-site have sparked researchers to further develop these family of materials for scintillator application.⁴

Recently, an all-inorganic copper-based metal halide Rb_2CuBr_3 developed as a scintillator achieved reported near-unity PLQY and $\sim 91,000$ photons/MeV radioluminescence-induced light yield using a low-cost, solution-based synthesis method.^{viii} However their slow response times in the μs timeframe is an issue for Cu-based imaging materials. A promising strategy to circumvent long lifetimes was recently revealed by Tang et al. with the replacement of the Cu cation with Ag in Rb_2AgBr_3 .^{ix} Here, it was proposed that broadband emission, large Stokes shift and sub-10 ns decay time originated from defect-bound exciton (DBE) luminescence. Described as excitons 'tightly bound to intrinsic or extrinsic defects', in this case the bromine vacancy V_{Br} which through first principles calculations was deemed as a fast and efficient radiative recombination centre. Subsequently, the peculiar photophysics of Ag-based metal halides led to investigations into analogues of Rb_2AgBr_3 such as Rb_2AgCl_3 ,^{x,xi} Cs_2AgX_3 ($X = \text{Cl}, \text{Br}, \text{I}$)^{xii,xiii,xiv} and $(\text{NH}_4)_2\text{AgX}_3$ ($X = \text{Br}, \text{I}$)^{xv}; the latter two offer comparisons between the halide species.

Kumar et al. published a study on Rb_2AgX_3 ($X = \text{Cl}, \text{Br}, \text{I}$) for anti-counterfeiting applications which were synthesised by solid-state reaction in an inert atmosphere. The optical characterisations revealed characteristic broadband emissions where Stokes shifts decreased with increasing anionic radii, $\text{Cl} > \text{Br} > \text{I}$. Time-resolved PL measurements exhibited lifetimes in the μs region, ranging from 0.62 to 1.15 μs . This differs from other literature on Rb_2AgX_3 where sub-10 ns lifetimes were reported which were instead synthesised from solution-based methods and physical vapour deposition.^{9,10-13} For both methods, there is a lack of comparison between the halide component whereby fast response times are recorded. Therefore, we report an in-depth evaluation on the material, optical and scintillation viability of both Rb_2AgCl_3 and Rb_2AgBr_3 for scintillator application via an optimised anti-solvent precipitation method to a high degree of purity. Furthermore, we investigated how the effect of applying pressure to compress powder into pellets impacted the luminescent properties. Pressure studies have been extensive on Pb-^{xvi} and Sn-based^{xvii} metal halides with PL emission which are determined by structural distortions. Here we report pressures ranging from 49.4 MPa to 499.4



MPa exerted on both Rb_2AgX_3 materials with changes recorded for the optical and radiation properties.

View Article Online
DOI: 10.1039/D5TC03935E

Results and Discussion

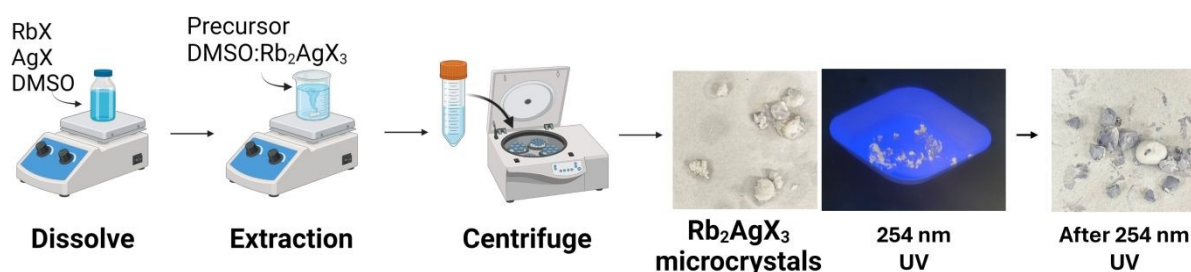


Figure 1: Schematic and results of the initial trial of ASP synthesis of Rb_2AgCl_3 adopted from Wu et al., including anti-solvent extraction and centrifugal isolation.

Wu et al. reported the synthesis of Rb_2AgCl_3 via anti-solvent precipitation using isopropyl alcohol (IPA) as the anti-solvent.¹¹ They dissolved the RbCl and AgCl precursors in DMSO and after heating, quickly injected the Rb_2AgCl_3 : DMSO coordinated solution into IPA to precipitate the Rb_2AgCl_3 product. Adopting this method, we found that this was successful when using bromide precursors as halogen, but not the chloride analogue. We successfully synthesised gram quantities of pure Rb_2AgBr_3 using this method, but due to difficulties with the solubility of AgCl , we could not make the chloride analogue in large quantities and instead were left with an impure product with lots of AgCl starting material.

The Kanatzidis Group found that solvent engineering was crucial for the isolation of different perovskite materials. Sidhik et al. 2022, conceived a solvent design principle to develop and characterise solution-processed 2D/3D halide perovskite bilayer structures.^{xviii} They controlled two solvent properties, the dielectric constant (ϵ_r) and the Gutmann donor number (DN), which regulates the coordination between the precursor ions and the solvent.^{xix} The Gutmann donor number (DN) is a Lewis affinity scale that was developed in the 1970s and is a good predictor of coordination affinity between precursor ions and the solvent, whereas the dielectric constant of solvents correlate to their relative polarity.^{xx} Tailoring both properties can allow for the successful isolation of desired perovskite materials. We looked at a range of anti-solvents with different DN and varying polarity that were most complementary to the primary solvent, DMSO, to obtain pure Rb_2AgX_3 ($X = \text{Cl}, \text{Br}$) scintillator materials.

Figure 2 plots the trialled anti-solvents based on their dielectric constant against their donor number, with those that successfully precipitated Rb_2AgX_3 highlighted. With Pb^{2+} -based



precursors DMSO is known to passivate uncoordinated Pb^{2+} defects.^{xxi} Thus, with Rb_2AgX_3 it has been assumed that DMSO coordinates to the Ag^+ centre via its sulfoxide lone pair acting as a Lewis acid. Protonated solvents disrupt the Lewis acid-base interaction by dissolving the Ag^+ coordination whereas aprotic solvents such as acetone and ethyl acetate (EtOAc) maintain the coordination, facilitating reaction.

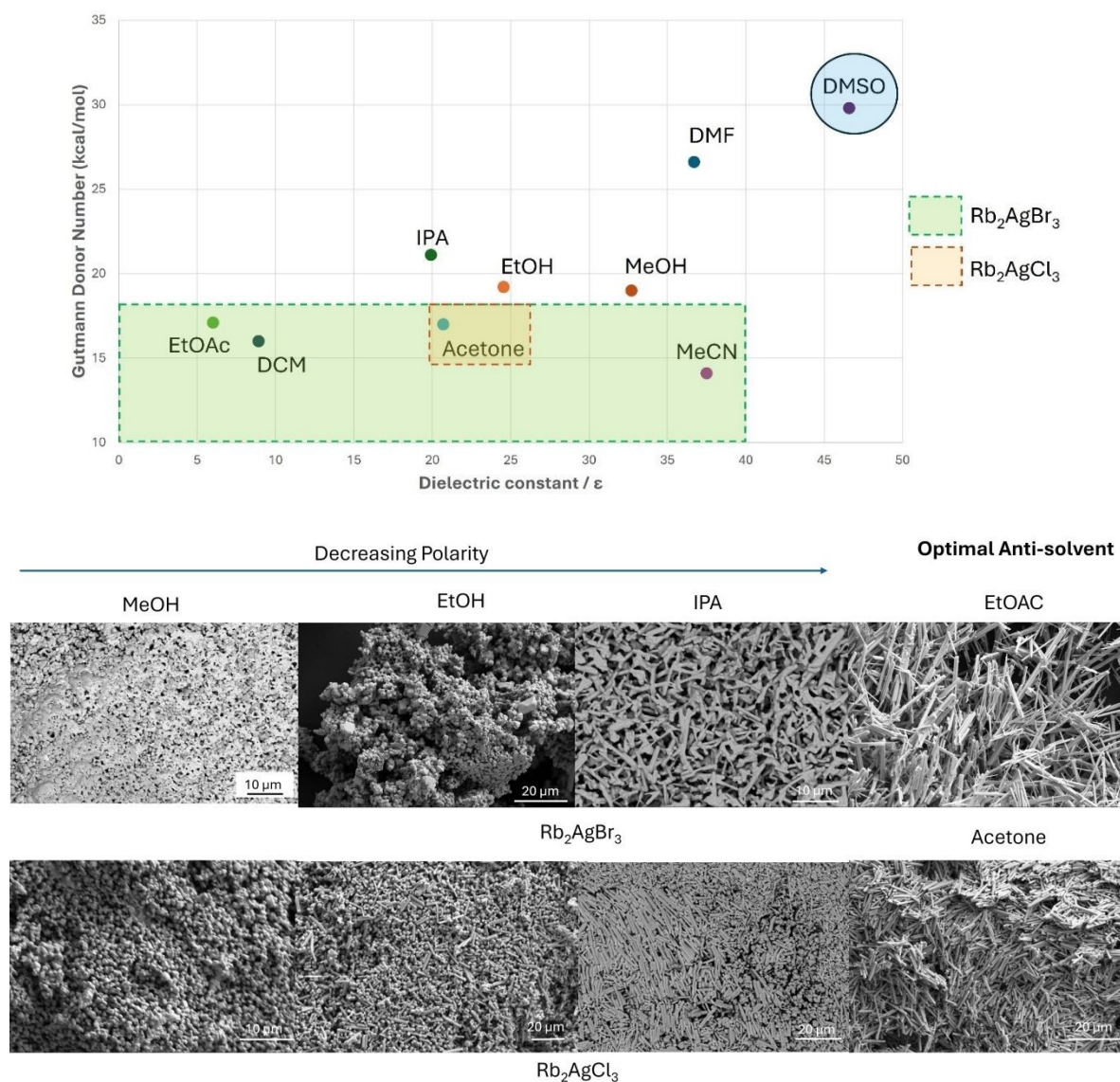


Figure 2. Plot of screened anti-solvents assessed on their dielectric constant versus Gutmann donor number with highlighted (green) area of solvents that successfully precipitated Rb_2AgX_3 . The coordinating solvent DMSO is also highlighted (blue), illustrating the strength of the Lewis base. BSE images of Rb_2AgX_3 powders from failed anti-solvents of decreasing polarity; from ethanol (MeOH), ethanol (EtOH) and propan-2-ol (IPA) vs optimal anti-solvents.

SEM imaging of the resulting Rb_2AgX_3 powders was used to substantiate the affinity towards aprotic, low-donor solvents, whereas protic solvents with higher polarity and donor number inhibit Rb_2AgX_3 crystallisation. Figure 2 illustrates this in BSE images that depict a



high degree of unreacted starting material as the polarity of the anti-solvent increases (IPA < EtOH < MeOH). Notably, Rb_2AgX_3 preferentially precipitate in differing solvents with the bromide in EtOAc and the chloride in acetone, suggesting differences in their solubility and thus affecting their anti-solvent induced crystallisation.

For Rb_2AgCl_3 , acetone was the only anti-solvent tested that resulted in a successful precipitation, as shown in Figure 2. The relatively high polarity of acetone ($\epsilon_{\text{Ace}} = 20.7$) succeeded in effectively disrupting the DMSO coordination with Ag^+ required for supersaturation, whereas EtOAc cannot extract Rb_2AgCl_3 as effectively. The higher polarity of acetonitrile (MeCN) ($\epsilon_{\text{MeCN}} = 37.5$) suggests that it should also precipitate the chloride product, however its lower donor capacity inhibits effective disruption of DMSO- Ag^+ coordination which corroborates the importance of donor number. SEM images in Figure 2 exhibit Rb_2AgCl_3 microcrystals that are littered with unreacted AgCl unless acetone is chosen as anti-solvent.

Rb_2AgBr_3 possesses the larger, more polarisable Br^- anion (compared to Cl^-) with decreasing solubility within a DMSO coordination. Thus, extraction of Rb_2AgBr_3 was facilitated by a solvent with low polarity which allows for both the steep change in solubility for supersaturation and is also not strongly miscible with DMSO. EtOAc (and DCM) have low polarity and strong Lewis basicity which is effective at precipitating out Rb_2AgBr_3 . Acetone and MeCN (acetonitrile) also allow precipitation of Rb_2AgBr_3 ; however, the high polarity affords greater miscibility with the DMSO coordination complex which may cause sporadic nucleation, resulting in crystal sizes of unequal sizes. For Rb_2AgBr_3 , EtOAc was found to be the optimal anti-solvent and for the Rb_2AgCl_3 product, acetone was the only solvent that successfully precipitated a pure material.

Powder X-Ray Diffraction

Having successfully obtained gram quantities of product (as white powders), powder X-ray diffraction (PXRD) allowed for confirmation of the crystal structure of Rb_2AgX_3 as well as an assessment on purity (Figure 3). By comparing the raw data to known reference patterns of Rb_2AgX_3 , (ICSD references 150287 = Br, 280031 = Cl) there was a strong match of diffraction peaks. The {101} and {102} crystal facets attributed to anisotropic 1D Rb_2AgX_3 materials were observed to be particularly intense at the 10.4° and 13.2° positions. These reflections are consistent with preferred orientation effects due to the needle-like morphology of the microcrystals, as observed in SEM imaging (see below). Comparing product diffraction patterns to reference patterns of the reagents showed a poor match confirming that Rb_2AgX_3 had successfully been synthesised to a high-level of purity. The stability in open-air was also monitored, as a major limitation to 1D Cu-based analogues was their deterioration in ambient



conditions, since copper experiences oxidation from Cu(I) to Cu(II).^{xxii} PXRD measurements were taken immediately following synthesis and again one month later, with no changes in the XRD pattern observed, indicating Rb_2AgX_3 retains sample purity in open-air storage (Figure S3, Supplementary Information).

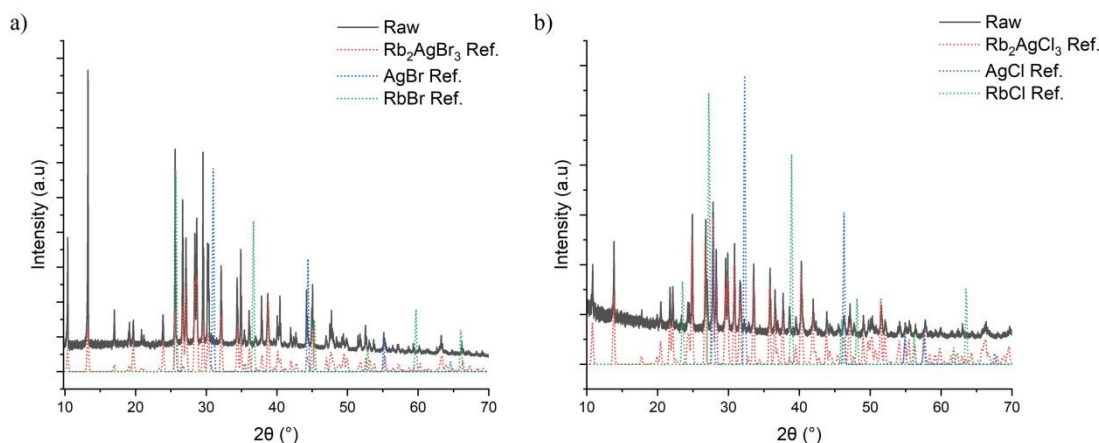


Figure 3. Powder X-Ray diffraction patterns of a) Rb_2AgBr_3 (b) Rb_2AgCl_3 overlaid with appropriate reference patterns sourced from the ICSD database.^{xxiii,xxiv}

Scanning Electron Microscopy (SEM) Imaging with Energy Dispersive Spectroscopy (EDS)

SEM imaging coupled with energy dispersive spectroscopy (EDS) highlights a uniform distribution of Rb, Ag and Cl/Br in the expected elemental ratios for the Rb_2AgX_3 products, which is further indication of the sample-purity offered by the optimised anti-solvent synthesis (Table 1 and Figure 4). The morphology of these materials is shown as 1D Rb_2AgX_3 rod-like crystals with electron images highlighting the size differences of the chloride product in comparison to the bromide as halogen. Measurement of the lengths and widths of Rb_2AgX_3 was carried out using ImageJ software, with a Gaussian distribution fitted to the data where $n = 100$, illustrated in Figure 4.^{xxv} For Rb_2AgCl_3 , the crystals exhibited greater uniformity with average sizes of $11 \mu\text{m} (\pm 3) \times 1.3 \mu\text{m} (\pm 0.3)$ compared to the bromide. Rb_2AgBr_3 showed more diversity in crystal sizes with averages of $25 \mu\text{m} (\pm 14) \times 2 \mu\text{m} (\pm 1)$.



Table 1. Energy dispersive spectroscopy (EDS) analysis of Rb_2AgX_3 confirming the chemical composition, deployed in tandem to SEM imaging. Article Online
DOI: 10.1039/D5TC03935E

Anti-Solvent	Rb_2AgBr_3	Rb_2AgCl_3
MeOH	AgBr (Ag = 58.9 %, Br = 40.6 %)	AgCl (Ag = 54.6 %, Cl = 45.1 %)
EtOH	$Rb_{1.28}AgBr_{2.55}$	AgCl (Ag = 40.5 %, Cl = 45.0 %)
IPA	$Rb_{1.36}AgBr_{2.67}$	$Rb_{1.21}AgCl_{1.81}$
EtOAc	$Rb_{2.01}AgBr_{3.01}$	$Rb_{1.14}AgCl_{1.76}$
DCM	$Rb_{1.96}AgBr_{2.98}$	$Rb_{1.08}AgCl_{1.97}$
Acetone	$Rb_{1.95}AgBr_{2.97}$	$Rb_{2.05}AgCl_{2.83}$
MeCN	$Rb_{1.99}AgBr_{2.93}$	AgCl (Ag = 39.7 %, Cl = 45.7 %)

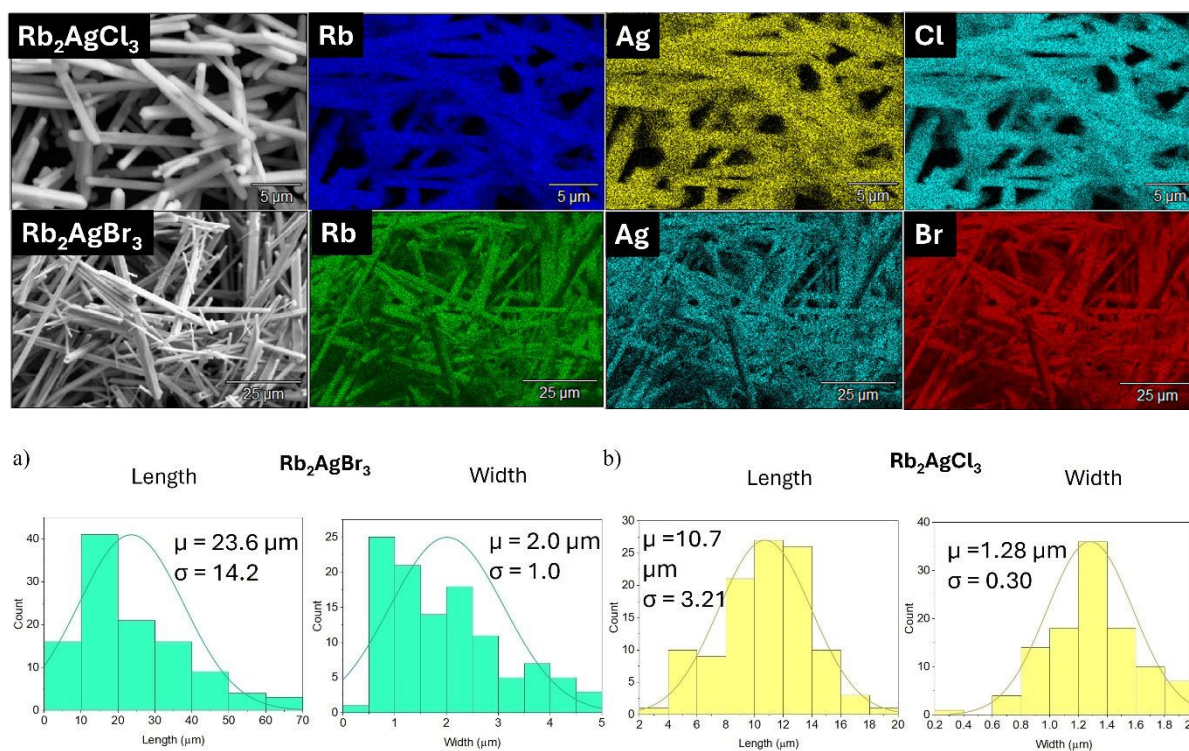


Figure 4. SEM images of Rb_2AgX_3 micro-crystals illustrating the elemental distribution of Rb, Ag and Cl/Br. A fitted Gaussian distribution of microcrystalline size dimensions (length and width) of a) Rb_2AgBr_3 and b) Rb_2AgCl_3 .

X-Ray Photoelectron Spectroscopy

X-Ray photoelectron spectroscopy (XPS) confirmed the valency of Rb_2AgX_3 , to ensure that no secondary phases were present. The magnified elemental core level spectra of both Rb_2AgX_3 are outlined in Figure 5 with the survey core-level spectra supplemented in **Error! Reference source not found.** Owing to the photosensitive nature of silver halide salts, rapid reduction to Ag(0) is experienced under the X-ray beam rendering assignment of peaks difficult. The Auger parameter (which is the energy difference between a photoelectron and Auger electron) allows differentiation between the chemical states of silver.^{xxvi} Fitting of the



silver 3d spectrum resulted in identification of two peaks at 368.2 and 374.4 eV (± 0.2), which is concordant with Ag^+ . Both Rb_2AgX_3 rubidium core-level spectra recorded a 3d doublet with binding energies at 109.7 eV and 110.2 eV (± 0.2) upon fitting, which is consistent with literature values and indicates that a Rb^+ environment is present.⁸ For Rb_2AgBr_3 , the chemical nature of the halide was determined to be Br^- as the 3d elemental spectrum possessed a convoluted peak which upon fitting revealed two maxima at 68.6 eV and 70.1 eV. In the 2p elemental spectrum, peaks of 198.1 and 200.1 eV correlate with a Cl^- chemical state. XPS measurements also allowed for the collection of a relative surface atomic profile of Rb_2AgX_3 , with the data summarised in **Error! Reference source not found.** and **Error! Reference source not found.**

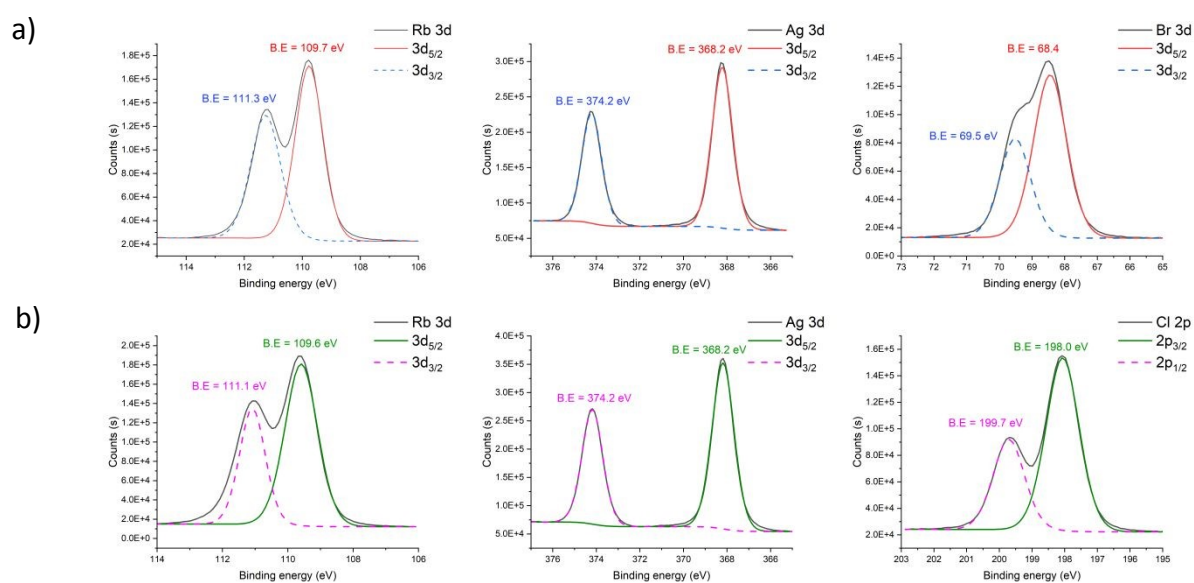


Figure 5. XPS elemental core level spectra for a) Rb_2AgBr_3 and b) Rb_2AgCl_3 accompanied by fitting modelled by Thermo Scientific™ Avantage software.

High Pressure XRD

The crystal structure of Rb_2AgX_3 products have been assigned the orthorhombic $Pnma$ space group. The unit cell structure is composed of tetrahedral $[\text{AgX}_4]^{3-}$ units packed along the b axis separated by Rb^+ cations (Figure 6). As shown by the reference unit cell parameters in **Error! Reference source not found.** (Supplementary Information), the tetrahedron units are more tightly packed in Rb_2AgCl_3 when compared to Rb_2AgBr_3 owing to the smaller atomic radius of chlorine.

In addition to solvent engineering for improved purity, crystal structure engineering was achieved by varying the halogen. X-ray diffraction patterns were collected at a range of



pressures (using a diamond anvil cell (DAC)) on single crystals of these materials. This compressibility comparison showed differences in the rigidity which is halogen dependent. Rb_2AgX_3 single crystal lattice parameters were measured at pressures from 0.43 to 4.05 GPa. At pressures higher than 4.05 GPa both samples recorded significant degradation. The web-based PASCAL (Principal Axis Strain Calculator) tool was used to analyse the anisotropic strain and compressibility, and each analogue was found to have a compression localised along differing axes including the [100], [010] and [001] crystallographic planes.

Table 2 summarises the calculated linear compressibility (β) values, which quantifies the shortening or expansion of the material per unit of applied pressure. The least compressible direction differs between the halides and is along the [001] plane, parallel to the *b*-axis for chloride, whereas for bromide it is along the [010] plane, parallel to the *c*-axis. Rb_2AgBr_3 shows greater rigidity along its AgBr_4 tetrahedral chains since they are stacked along the [010] plane, whereas this is the most compressible direction for the chloride version. Bulk modulus figures indicate that the Rb_2AgCl_3 crystal structure has a stiffer lattice than the bromide crystal, and Rb_2AgBr_3 is measured to have a 'softer' lattice with a lower bulk modulus. Similar results were recently calculated by Tang *et al.* with calculated stiffnesses of both materials in good agreement with our experimental results.^{xxvii}

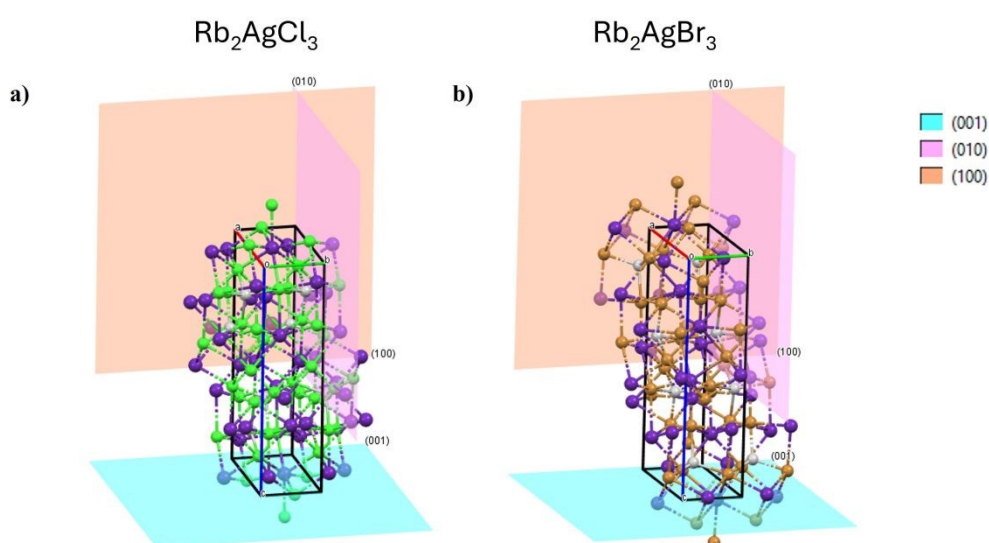


Figure 6. *Pnma* unit cells of a) Rb_2AgCl_3 and b) Rb_2AgBr_3 crystals labelled with the compressed crystallographic axes of [100], [010] and [001] modelled with MercuryTM software by the Cambridge Crystallographic Data Centre.

Table 2: Linear compressibility and bulk modulus of Rb_2AgCl_3 and Rb_2AgBr_3 .



Property	Crystallographic Plane / <i>hkl</i>	Rb ₂ AgCl ₃	Rb ₂ AgBr ₃
Linear Compressibility (TPa ⁻¹)	(100)	12.2	18.0
	(010)	16.2	12.0
	(001)	8.82	15.0
Bulk Modulus / GPa (This work)	—	19.5	17.5
Bulk Modulus / GPa (Literature) ²⁵²	—	18.3	15.6

View Article Online
DOI: 10.1039/C5TC03935E

Optical Comparison

The optical properties of Rb₂AgX₃ were investigated via room-temperature photoluminescence (PL) spectroscopy. Excitation (PLE) and emission (PL) spectra for the polycrystalline powdered Rb₂AgX₃ materials are shown in Figure 7 and show blue-shifted emission when changing from Cl to Br, which contrasts with conventional MHPs such as CsPbX₃, Cs₂ZrX₆, etc. Rb₂AgBr₃ exhibits two excitation centres at 263 nm (4.71 eV) and 286 nm (4.33 eV). The dominant excitation peak at 263 nm resulted in broadband emission centred at 514 nm (2.41 eV) giving a large Stokes shift of 251 nm. The weaker excitation peak at 286 nm leads to very weak broadband emission at 365 nm (3.39 eV), with a lower Stokes shift of 63 nm (0.71 eV). Kumar *et al.* also observed two PL emission peaks from Rb₂AgBr₃ with the higher energy emission at 363 nm.¹⁴ This very weak high energy bromide emission mechanism has been attributed to self-trapped exciton (STE) behaviour whereas the dominant peak at 514 nm (2.4 eV) is assigned to emission from defect bound excitons (DBE), which aligns well with the energy of Br₂ vacancies calculated by Kumar *et al.*¹⁴ Since STE emission is caused by temporary distortions in the excited state of the molecule, this process is not expected to affect the ground state spectrum. This is verified by the excitation spectrum of Rb₂AgBr₃ measured at an emission wavelength of 363 nm, which shows no features (Figure 7a).

Rb₂AgCl₃ possesses a sharp excitation peak centred at 247 nm (5.02 eV) with resulting emission recorded at 585 nm (2.12 eV), giving a large Stokes shift of 338 nm (2.90 eV). The energy difference of Rb₂AgBr₃ compared to Rb₂AgCl₃ is attributed to the different atomic size of the halogens altering the crystal lattice and changing the bandgap.^{xxviii} The broad nature of these PL peaks has been attributed to metastable halogen vacancies which likely relate to the abundant defects found with silver halides.^{xxix} Rb₂AgBr₃ can exhibit a dual emission mechanism, although the higher energy PL peak at 363 nm assigned to STE-based emission is very weak suggesting only a minor population undergo this process, with the majority of Rb₂AgBr₃ charge carriers associated with bromine vacancy V_{Br} bound excitons. Kumar *et al.* proposed that the excitation energy can be transferred from STEs to DBEs in Rb₂AgBr₃ whereas for Rb₂AgCl₃, STE energy is completely quenched by the defects.¹⁴



Variable temperature PL emission spectra are also shown in Figure 7. Rb_2AgBr_3 displays enhanced emission intensity that is red shifted (lower energy) as the temperature decreases from room temperature to 79 K (Figure 7e). This suggests that non-radiative recombination is suppressed at low temperatures which explains the lower PL emission intensity of Rb_2AgBr_3 at room temperature compared to the chloride version. The opposite trend is observed for Rb_2AgCl_3 (Figure 7f) where the emission intensity decreases as the temperature decreases until 179K (and below) where a new high energy band appears due to a mid-gap state.

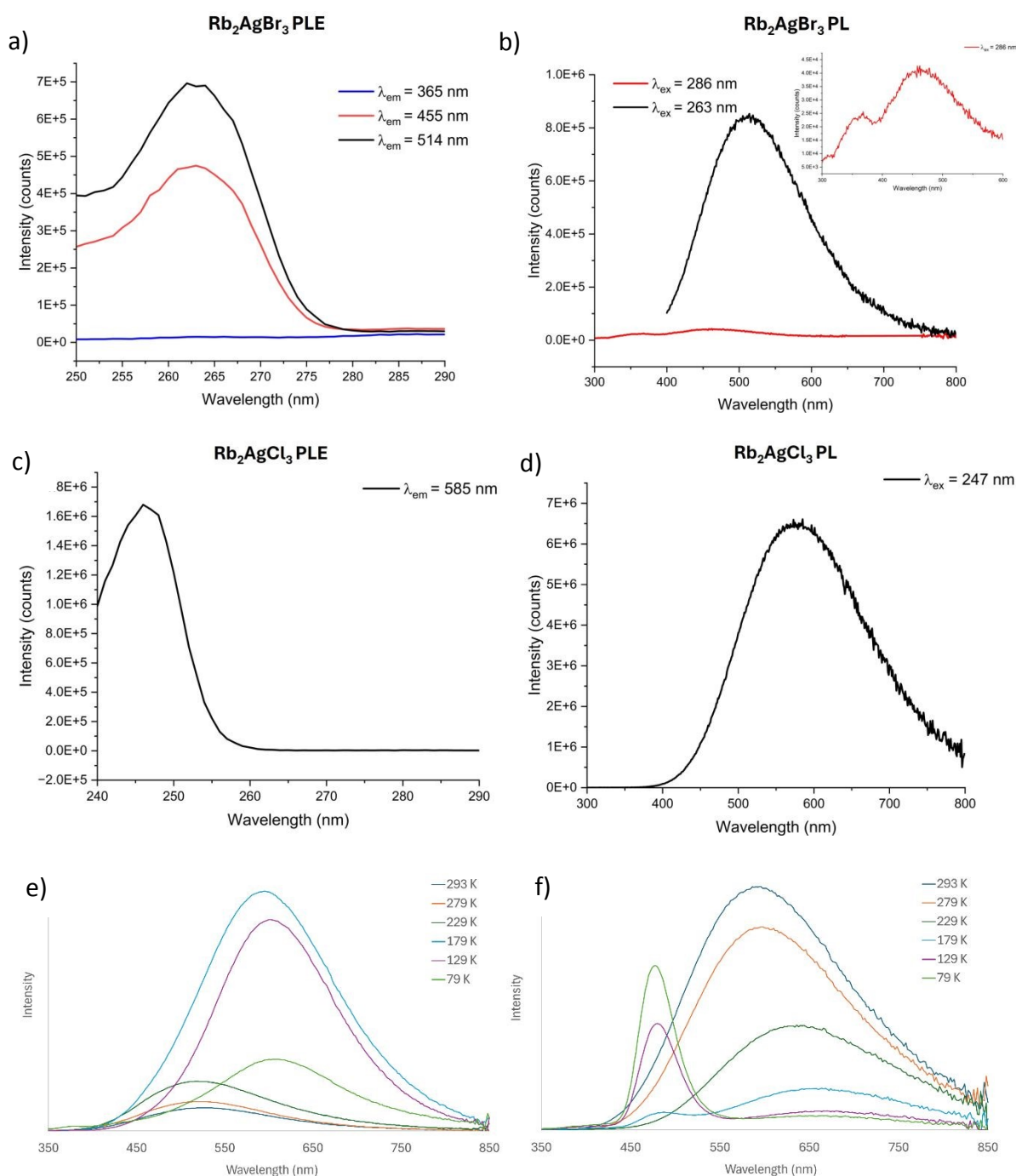


Figure 7. The photoluminescence excitation (PLE) spectra (a, c) and photoluminescence (PL) spectra (b, d) of Rb_2AgX_3 ($X = \text{Br}, \text{Cl}$) powders, showing distinct excitation and emission features for each



halide; inset highlights the PL emission of Rb_2AgBr_3 at $\lambda_{\text{ex}} = 286 \text{ nm}$. Variable-temperature spectral measurements of (e) Rb_2AgBr_3 and (f) Rb_2AgCl_3 powders. Measurement parameters: $\lambda_{\text{ex}} = 260 \text{ nm}$ for Rb_2AgBr_3 and $\lambda_{\text{ex}} = 248.5 \text{ nm}$ for Rb_2AgCl_3 .

Rb_2AgCl_3 enjoys a considerably higher PLQY (30.21 %; measured at 247 nm excitation) than the bromide analogue (4.78 %; measured using 266 nm excitation), again indicating that a higher fraction of excitons is lost to non-radiative transfer in the bromide material in agreement with the temperature dependent emission spectra (Figure 7). Tang *et al.* proposed that the DBE emission pathway results from light-induced excitons transferring to the end of $[\text{AgX}_4]^{3-}$ chains and binding to the halogen vacancies.²⁷ The optical properties of both materials were maintained for at least 12 months, since multiple measurements gave similar emission data (Figure 7).

Scintillation comparison of Rb_2AgX_3

To understand the scintillation behaviour of Rb_2AgX_3 under ionizing radiation, X-ray radioluminescence (RL) measurements were carried out on both Rb_2AgBr_3 and Rb_2AgCl_3 with the resultant spectra shown in Figure 8. Similarly to the PL profiles, the powder maintained the characteristic broadband shape with emission centred at 520 nm (Rb_2AgBr_3) and 585 nm (Rb_2AgCl_3) with no deterioration observed over the course of 12 months.

The unique excitonic behaviour is further shown with time-resolved radioluminescence (TRRL) measurements. Figure 8 gives time-resolved spectra of both Rb_2AgX_3 , highlighting their ultra-fast decay (Table 3). Rb_2AgBr_3 exhibits a very-fast lifetime component of 4.4 ns with a slower component of 232.2 ns. The data for Rb_2AgCl_3 also shows a fast 6.0 ns lifetime. Time-resolved PL measurements are in good agreement with the TRRL results (Table 3). As previously reported, sub-10 ns lifetimes are characteristic of Rb_2AgX_3 as they reflect the dominance of the DBE emission pathway. Self-trapped excitons are characterised by decay lifetimes in the μs range as seen with analogous metal halides such as Rb_2CuX_3 .^{8, xxx} Such long decay times are a limitation as it would hinder scintillation response times during X-ray imaging.²



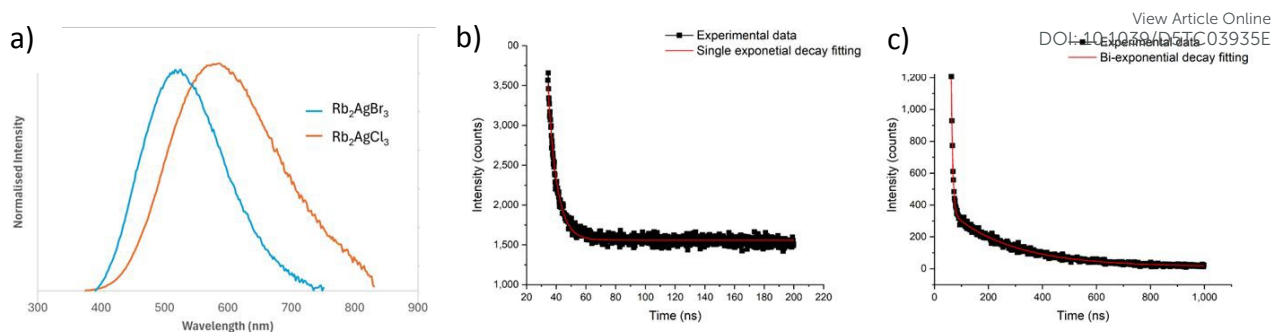


Figure 8. a) Radioluminescence spectrum of Rb_2AgBr_3 and Rb_2AgCl_3 powder under 40 kV, 300 μA X-ray source. Time-resolved RL spectra of b) Rb_2AgCl_3 overlaid with single exponential decay fitting and c) Rb_2AgBr_3 fitted with a bi-exponential decay fitting.

Table 3. Lifetime components derived from single and biexponential fitting of time-resolved radioluminescence (TRRL) and photoluminescence (TRPL) measurements of Rb_2AgBr_3 and Rb_2AgCl_3 , respectively.

Rb_2AgX_3	TRRL Lifetime Components			
	τ_1 / ns	A_1	τ_2 / ns	A_2
Rb_2AgBr_3	5.7	4.9×10^7	232.2	439.9
Rb_2AgCl_3	6.0	5.8×10^5	N / A	N / A
	TRPL Lifetime Components			
	τ_1 / ns	A_1	τ_2 / ns	A_2
Rb_2AgBr_3	5.5	1.3	197	3.7×10^{-2}
Rb_2AgCl_3	1.1	7.5×10^{-2}	4.7	1.8×10^{-2}

Figure 9 illustrates the linearity of the Rb_2AgX_3 scintillator response as a function of increasing X-ray current. The Rb_2AgBr_3 sample has a stronger scintillation photocurrent than Rb_2AgCl_3 , consistent with either a higher light yield or higher effective density. By comparing the gradient of the linear fits to this data, the light yield of powdered Rb_2AgBr_3 is calculated to be 36% that of BGO (equivalent to approximately 3600 photons/MeV) and the light yield of powdered Rb_2AgCl_3 is 15% that of BGO (equivalent to approximately 1500 photons/MeV). Figure 9 shows the mass attenuation coefficients for each material as a function of X-ray energy, which confirms that the attenuation is very similar for both Rb_2AgBr_3 and Rb_2AgCl_3 (and also for BGO) at the mean X-ray energy of 35 keV.



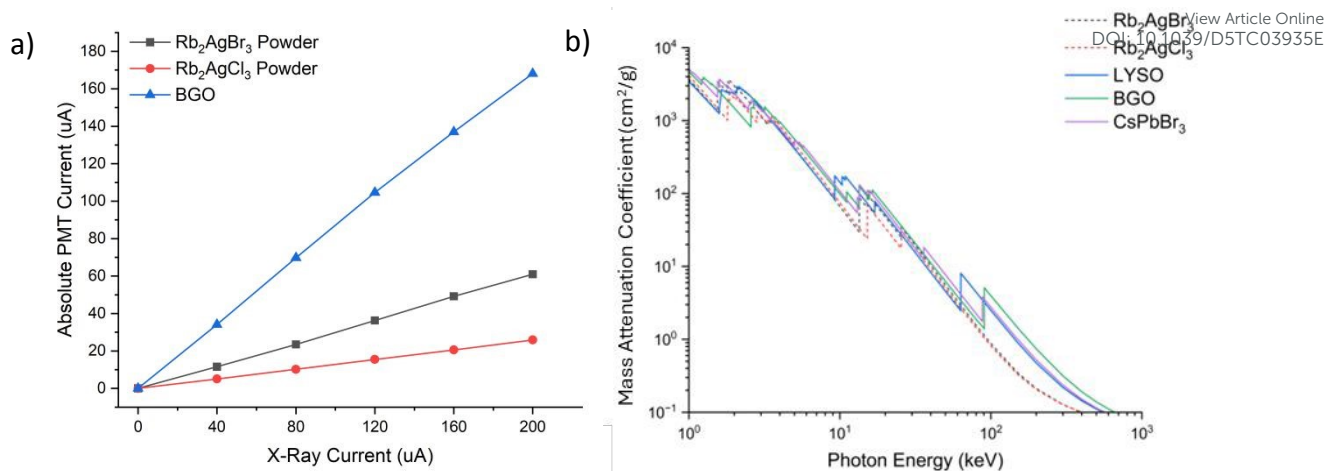


Figure 9. a) A comparison of as-synthesised Rb_2AgX_3 response to increasing X-ray current as measured by a PMT versus a known commercial scintillator standard, BGO. A b) mass attenuation plot of Rb_2AgX_3 versus known commercial scintillators and $CsPbBr_3$.

While conventional MHs such as $CsPbBr_3$ have high optical efficiency, Rb_2AgBr_3 offers a non-toxic alternative with superior stability while maintaining X-ray attenuation albeit with a lower light yield. $Cs_3Cu_2I_5$ has a higher light yield but a much slower decay (microsecond level) and lower thermal stability. Cation doping has been shown to be effective in enhancing the light yield, e.g. Mn^{2+} doping of $Cs_2CdBr_2Cl_2$, however high doping levels can lead to non-radiative processes and slow decay.^{xxxix} Cu^+ doping of Rb_2AgBr_3 , Rb_2AgI_3 and Cs_2AgI_3 has been shown to give higher light yields than without doping, and while doping with Cu^+ does slow decay times, this can be minimised by using trace doping levels.^{xxxix} Gui et al have recently published increased PLQY with Li^+ doped Rb_2AgCl_3 scintillator while maintaining suitable ns decay times.^{xxxix}

Pressure effects on pellets of Rb_2AgX_3

To function as a device, the polycrystalline powders need to be in a functional format such as a film or compact pellet. Rb_2AgX_3 powders were compacted into pellets at various pressures as shown below.



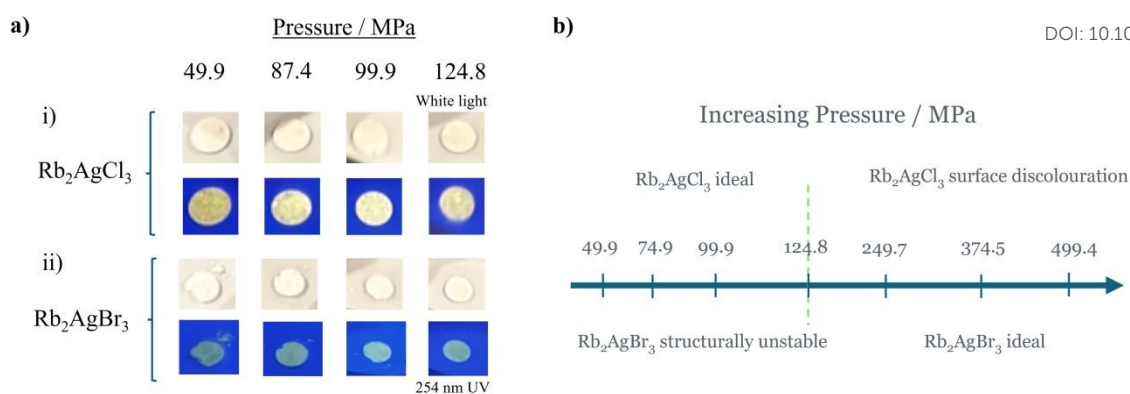


Figure 10. a) Diagram of ideal pressure range for pressing Rb_2AgX_3 pellets b) Images of Rb_2AgX_3 10 mm diameter \varnothing pellets pressed under pressures ranging from 124.8 MPa to 499.4 MPa and those under heat-treatment under 251 nm UV.

To assess the ideal pressure range for each of the Rb_2AgX_3 powders, an extensive range was covered as illustrated in Figure 10. Initially, low pressures covering 49.9 to 124.8 MPa were trialled with differing results for both materials. Rb_2AgCl_3 was able to form clean, stable pellets whereas the bromide analogues were not structurally viable. Increasing pressures to 499.4 MPa led to stable Rb_2AgBr_3 pellets however for the chloride, surface discolouration appeared above 124.8 MPa. This was due to residual DMSO left in the powders. Despite the darkened surface, luminescence from the pellet was still maintained as seen in Figure 10. The range of 124.8 to 499.4 MPa was chosen as the most suitable for comparing optical and scintillation properties of Rb_2AgX_3 pellets because both halides were stable in this range.

To further elucidate the changes in brightness with increasing pressure, PL measurements of the pellet series for both materials were conducted. Table S4 summarises the PL data for both series of Rb_2AgX_3 pellet series at their dominant excitation wavelength; 247 nm for Rb_2AgCl_3 and 263 nm for Rb_2AgBr_3 , with PL spectra shown in Figure S4. For PL, Rb_2AgCl_3 continues to be the brighter of the two materials after the application of pressure. The general trend shows improved PL emission of pellets compared to powdered analogues.

Backscatter SEM imaging of cross-sections of the pellets (Figure S7) show changes in the morphology of Rb_2AgX_3 with increasing pressure. Rb_2AgX_3 has less needle-like morphology as pressure increased from 124.8 to 499.4 MPa due to a reduction in voids. Pressurising powder into pellets reduced voids and compacted grain boundaries resulting in an improvement of PL intensity. Similar results were reported where Wang et al. investigated pressure-induced PL enhancement of the 1D hybrid metal halide material $C_4N_2H_{14}PbBr_4$, revealing that improvement in PL intensity and PLQY was because of the suppression of non-radiative decay losses.^{xxxiv}



Comparing the PL data of the powder to the pellet series, there is a slight red shift in the bandgap (λ_{\max} values) under increasing pressure. Rb_2AgCl_3 experiences a red shift under increasing pressure from 585 nm to 594 nm, while for Rb_2AgBr_3 , the pressure applied had less of an impact with smaller changes of the λ_{\max} positions, albeit with both peaks retaining very broad emission (Table S4 and Figure S4).

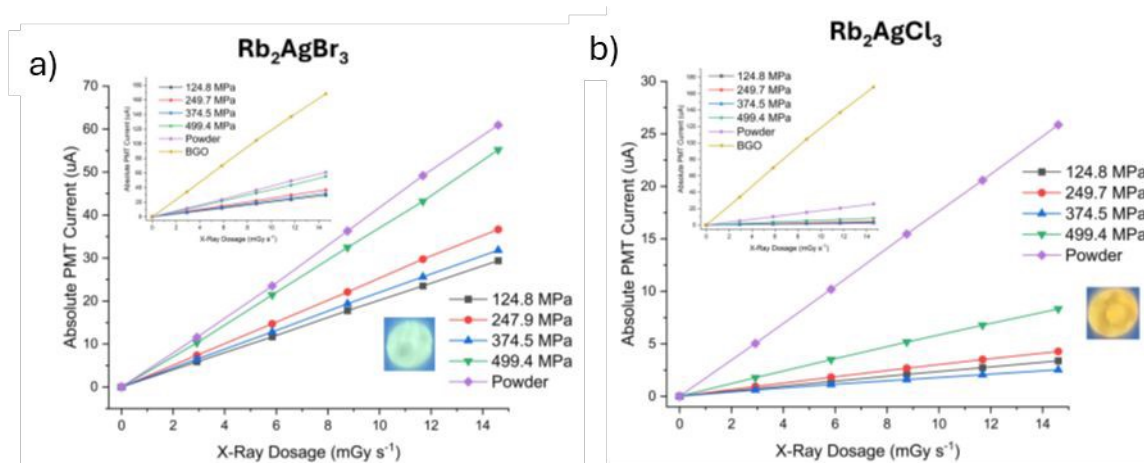


Figure 11: X-Ray sensitivity measurements of pellets versus as-synthesised powder. a) Rb_2AgBr_3 under increasing pressure and b) Rb_2AgCl_3 under increasing pressure. Included in inset graphs are comparisons of the data to commercial standard BGO.

The assessment of the scintillator performance of the pellet series is shown in Figure 11 and again a linear response was recorded under increasing X-ray current. After the pellets had been subjected to pressure treatment, measurements show that Rb_2AgBr_3 elicited a stronger current response under increasing X-ray current compared to Rb_2AgCl_3 . For both materials when subject to pressure alone, the best response was recorded at 499.4 MPa, encouragingly for Rb_2AgBr_3 the response was comparable to the powder. These results show promise of a correlation with increasing pressure and improved X-ray sensitivity offering a route of future exploration into higher pressure studies. Combining this with appropriate doping of these lead-free materials may facilitate high performance thick film scintillation.

Conclusion

In conclusion, this paper has explored the suitability of metal halides for scintillator application by examining the promising lead-free candidates: Rb_2AgCl_3 and Rb_2AgBr_3 . An improved solution-based synthesis was developed by optimising solvent/anti-solvent interaction, subsequently confirmed by both PXRD and EDX analysis. This low-cost synthesis offers a favourable alternative to those using corrosive acids, time consuming crystallisation or resource-intensive solid-state methods. PL spectroscopy of the Rb_2AgX_3 powders allowed



quantitative optical comparison via for the first time, revealing the chloride to be brighter than the bromide analogue by a factor of 10. Under scintillation characterisation X-ray sensitivity measurements revealed that the bromide produced a stronger response than the chloride as halogen. One of the most promising findings of these materials are the sub-10 ns decay times recorded in TRRL, 5.8 ns for Rb_2AgBr_3 and 6.0 ns for Rb_2AgCl_3 . Ideal for dynamic X-ray imaging, this solution-based method does not hinder decay time performance.

The effect of compressing the powder into pellets under pressures ranging from 124.8 to 499.4 MPa showed a general trend of PL intensity increasing upon application of pressure. X-ray sensitivity measurements also revealed an improvement in performance with increasing pressure.

Data Availability

The data supporting this article have been included as part of the Supplementary Information. Single crystal structure data in this work are available in the Inorganic Crystal Structure Database (ICSD), under deposition numbers CSD 2498636-2498649.

Conflict of Interest

There are no conflicts of interest.

Acknowledgements

RM acknowledges studentship funding from the University of Surrey Doctoral College. JG acknowledges support from the "NuSec" Nuclear Security Science Network managed by the University of Surrey and funded by the STFC, Grant ST/S005684/1, and from the Defense Threat Reduction Agency (DTRA) IIRM University Research Alliance under award no. HDTRA1-20-2-0002. The authors would like to acknowledge funding for the EPSRC UK National Crystallography Service (EP/W021129/1).

Experimental

Chemicals

Rubidium bromide (99.8 %, Alfa Aesar), rubidium chloride (99.8 %, Alfa Aesar), silver bromide (99.9 %, Alfa Aesar) silver chloride (99.8 %, Alfa Aesar), dimethyl sulfoxide (Fisher Chemical), ethyl acetate (99+%, Sigma-Aldrich), acetonitrile (99.6+%, Sigma-Aldrich), methanol (99.8+%, Sigma-Aldrich), ethanol (96%, Sigma-Aldrich), n,n-dimethylformamide (99.8 %, Thermo Scientific), propan-2-ol (99.5 % Sigma-Aldrich) and acetone (>99 %, Sigma-Aldrich) were purchased and used as received.



Synthesis Method

Rb_2AgX_3 ($X = \text{Cl}, \text{Br}$) was successfully synthesised via an optimised low-temperature solution growth method; adapted and modified from Han et al., 2022.^{xxxv} The precursor solution was prepared by mixing 20 mmol of RbX and 10 mmol of AgX into 200 mL of DMSO. The solution was heated to 60 °C for 4 h until all solute had dissolved, resulting in a clear solution. Subsequent filtering via PVDF membrane filters with 0.45 μm pore size allowed adequate removal of impurities. The next stage involved quickly injecting aliquots of the Rb_2AgX_3 : DMSO solution into the appropriate anti-solvent, resulting in the precipitation of Rb_2AgX_3 . The ideal conditions of the extraction were found to be 1 mL aliquot additions to 40 mL anti-solvent whilst stirring at 1000 RPM. The white Rb_2AgX_3 precipitate is collected via vacuum filtration then dried at 40 °C under vacuum overnight.

Material Characterisation

X-ray Diffraction

PXRD patterns were obtained with a Malvern Panalytical X'Pert powder diffractometer at 45 kV and 40 mA with a $\text{Cu K}\alpha = 1.5406 \text{ \AA}$ target source. Measurements were collected between 2θ angles of 10 ° and 70 ° at a 0.002 step size over a 40-minute period. Reference patterns were sourced from the Inorganic Crystal Structure Database.

X-ray Photoelectron Spectroscopy

XPS measurements were performed via a Thermo Scientific K-Alpha⁺ spectrometer with a monochromatic $\text{Al K}\alpha$ ($h\nu = 1486.6 \text{ eV}$, $1 \text{ eV} = 1.6 \times 10^{-19} \text{ J}$) X-ray source. An X-ray spot of ~ 400 μm radius was employed in the acquisition of spectra. Elemental survey spectra were collected via a pass energy of 300 eV with high-resolution, core-level spectra employing a pass energy of 50 eV. Subsequent data fitting was performed through the manufacturer's software AdvantageTM as well as incorporating the necessary sensitivity factors and correction for the electron analyser transmission function.

Scanning Electron Microscopy

Scanning electron microscopy (SEM) analysis was performed via a Thermo Scientific Apreo S electron microscope. Both secondary electron and backscatter images were collected via ETD and T1 detectors respectively, at a range of beam energies 7 - 10 kV at 0.8 - 1.6 nA beam currents. Energy-dispersive X-ray (EDX) spectroscopy measurements were performed in tandem, collecting spectra and elemental distribution mapping. All samples were sputter coated in 3 nm thick Au coating to promote sample conductivity.

Thermogravimetry and Differential Scanning Calorimetry

Thermogravimetric analysis was performed on Rb_2AgX_3 powders (5 - 7 mg), placed in a quartz crucible under a nitrogen atmosphere using a TGA Q500 instrument from TA Instruments (New Castle, USA). The temperature was ramped from room-temperature to 1000 °C at a 10 °C min^{-1} rate. Differential scanning calorimetry was performed via a DSC Q1000 (TA Instruments) that was calibrated with indium. Approximately 5 - 7 mg of powder was placed into an aluminium crucible and hermetically sealed along with another empty crucible acting as the reference. The temperature was also ramped from room-temperature to 1000 °C at a 10 °C min^{-1} rate under a nitrogen atmosphere.



Optical and Scintillation Characterisation

View Article Online
DOI: 10.1039/D5TC03935E

Photoluminescence Spectroscopy

PL measurements on powders were performed on an FLS1000 Photoluminescence Spectrometer (Edinburgh Instruments Ltd., Livingston, UK), with double excitation and emission monochromators. Emission was detected with a visible PMT-900 detector. Variable-temperature PL measurements were performed in a liquid nitrogen-cooled Optistat cryostat (Oxford Instruments Nanoscience plc., Abingdon, UK). Spectral measurements were performed under excitation from a Xe lamp. Time-correlated single photon counting and multichannel scaling measurements were performed under excitation at 280 nm by an EPLED-280 picosecond pulsed LED source, and at 255 nm by an VPLED-255 variable pulse LED source respectively. Determination of lifetimes was performed by reconvolution fitting methods. Absolute photoluminescence quantum yield (PLQY) measurements were performed by direct methods under Xe lamp excitation with a QYPro Integrating Sphere (Edinburgh Instruments Ltd., Livingston UK). PL measurements on pellets were performed on an FLS980 Photoluminescence Spectrometer (Edinburgh Instruments) under excitation from a Xe lamp.

X-ray Induced Radioluminescence spectral measurements

Spectral RL measurements on powders were performed in an XS1 RL Chamber (Edinburgh Instruments Ltd., Livingston, UK) under excitation from a 12 W continuous wave X-ray source (target = Tungsten) (MOXTEK Inc., Orem, USA). The voltage and current of the source were varied from 10 – 40 kV and 2.5 – 300 μ A respectively. RL emission was collected by a liquid light guide coupled to the FLS1000 spectrometer. Emission was detected with a visible PMT-900 detector.

Time-resolved Radioluminescence Spectroscopy

Time-resolved radioluminescence (TRRL) measurements were performed at the University of Cambridge by Dr Hayden Salway. Spectra were collected via a FLS1000 photoluminescence spectrophotometer (Edinburgh Instruments) coupled to a 40 kV X-ray source (Hamamatsu Photonics N5084).

X-ray Sensitivity

X-ray sensitivity data was collected via an X-ray source (Amptek Mini X-2) at 50 kV where the beam passed through a 5mm diameter. Rb_2AgX_3 samples were held at a 10 cm distance from the collimator with emitted light collected at 90° via a 2 in diameter PMT detector (ET Enterprises 9256B). Measurements were obtained under a range of currents between 40 – 200 μ A at 40 μ A incremental steps. To minimise the effect of background noise, the system was encased in a lead-lined, light-tight box that was sealed with measurements taken in a dark room.

HPXRD Experimental section

High pressure data for Rb_2AgX_3 (X = Cl, Br) were collected at 293(2) K on a Rigaku XtaLAB Synergy-S diffractometer equipped with an Oxford Cryosystems Cryostream open-flow cooling device using mirror monochromated Mo K α radiation ($\lambda = 0.71073 \text{ \AA}$), generated using a microfocus sealed X-ray tube source and detected at a HyPix Arc-100 Detector. A crystal of Rb_2AgCl_3 (colourless block) was cut to dimensions of approximately $0.05 \times 0.07 \times 0.23 \text{ mm}$



and studied in Daphne-7575 at pressures of 0.0001, 0.43(5), 1.45(5), 2.55(5), 3.56(5) and 4.05(5) GPa. A crystal of Rb₂AgBr₃ (colourless block) was cut to dimensions of approximately 0.03 × 0.04 × 0.13 mm and studied in Daphne-7575 at pressures of 0.0001, 0.69(5), 1.25(9), 1.86(7), 2.46(5), 3.23(5) and 4.05(5) GPa, with viable datasets suitable for structural analysis obtained up to 3.23(5) GPa. The hydrostatic limit of Daphne-7575 is reported to be approximately 4 GPa.^{xxxvi,xxxvii}

The sample chambers of the two screw Merrill-Bassett diamond anvil cells (DACs) used to conduct the HPXRD experiments were formed by two 800 μm culet faces of Boehler-Almax diamonds fitted into tungsten carbide backing seats. Stamped steel sheets (thickness 250 μm) were indented to a thickness of approximately 130 μm using the diamond anvils. Gasket holes were drilled using a BETSA electric discharge machine fitted with a 380 μm diameter tungsten electrode. The sample crystals were fixed to one culet face by means of high vacuum hydrocarbon grease alongside ruby spheres, which allowed for pressure measurement using the ruby fluorescence method.^{xxxviii} After each pressure ramp, the pressure inside the DACs were allowed to equilibrate for a minimum of 24 hours before data collection was initiated. Pressure measurements were taken immediately before and after each collection and the pressure reported as the average, plus 0.05 GPa attributed to the inherent uncertainty of the pressure determination via the ruby fluorescence method.^{xxxix}

Cell refinement and data reduction were carried out using the software CrysAlisPRO.^{xl} Special settings (DAC opening angle, dataset resolution limits, profile rejection parameters and regular background updates) were implemented in the data reduction step, which helped remove contaminating diamond reflections and powder rings from the data. Individual specifications of the exact settings used are contained within the crystallographic information files in the field '_diffn_special_details'. For the ambient pressure collections, numerical absorption corrections were applied therein using Gaussian integration over multifaceted crystal models.^{xli} For the high pressure collections, multi-scan absorption corrections were applied with an empirical absorption correction using spherical harmonics, as implemented in the SCALE3 ABSPACK scaling algorithm^{xlii} through CrysAlisPRO. The initial collections conducted outside of the DAC at ambient pressure were solved using SHELXT^{xliii} through the Olex2 interface^{xliv} and all high pressure datasets conducted inside the DAC were solved by importing a reference model from either this ambient pressure collection or an appropriate model from the previous lower pressure point. All structural refinements were carried out using SHELXL^{xlv} through the Olex2 interface. Single crystal structure data in this work are available in the Inorganic Crystal Structure Database (ICSD), under deposition numbers CSD 2498636-2498649.

References

- ⁱ B. D. Milbrath, A. J. Peurrung, M. Bliss and W. J. Weber, *J Mater Res*, 2008, 23, 2561–2581.
- ⁱⁱ Y. Zhou, J. Chen, O. M. Bakr and O. F. Mohammed, *ACS Energy Lett*, 2021, 6, 739–768.
- ⁱⁱⁱ A. Jana, S. Cho, S. A. Patil, A. Meena, Y. Jo, V. Gopalan Sree, Y. Park, H. Kim, H. Im, R. A. Taylor, *Materials Today*, 55, 2022, 110-136.
- ^{iv} Y. Tang, S. Tang, M. Luo, Y. Guo, Y. Zheng, Y. Lou, Y. Zhao, *Chem. Commun.*, 2021, 57, 7465-7479.
- ^v G. Kakavelakis, M. Gedda, A. Panagiotopoulos, E. Kymakis, T. D. Anthopoulos, K. Petridis, *Advanced Science* 2020, 7, 2002098.



- vi H. Huang, L. Polavarapu, J. A. Sichert, A. S. Sussha, A. S. Urban and A. L. Rogach, *NPG Asia Mater*, 2016, 8, e328–e328.
- vii C. Zhou, H. Lin, Q. He, L. Xu, M. Worku, M. Chaaban, S. Lee, X. Shi, M.-H. Du and B. Ma, *Materials Science and Engineering: R: Reports*, 2019, 137, 38–65.
- viii B. Yang, L. Yin, G. Niu, J.-H. Yuan, K.-H. Xue, Z. Tan, X.-S. Miao, M. Niu, X. Du, H. Song, E. Lifshitz and J. Tang, *Advanced Materials*, 2019, 31, 1904711.
- ix M. Zhang, X. Wang, B. Yang, J. Zhu, G. Niu, H. Wu, L. Yin, X. Du, M. Niu, Y. Ge, Q. Xie, Y. Yan and J. Tang, *Adv Funct Mater*, 2021, 31, 2007921.
- x Z. Zhang, X. Guo, K. Huang, X. Sun, X. Li, H. Zeng, X. Zhu, Y. Zhang and R. Xie, *J Lumin*, 2022, 241, 118500.
- xi D. Wu, Y. Luo, P. He, K. An, J. Lai, P. Feng, M. Zhou, Y. Liu, X. Tang and G. Han, *ACS Applied Optical Materials*, 2023, 1, 78–84.
- xii J.-L. Yao, Z.-X. Zhang, X.-Q. Sun, T. Chang, J.-F. Guo, K.-K. Huang, H.-B. Zeng, D.-Y. Wang, W.-S. Yang, R.-S. Zeng, X.-M. Li and R.-G. Xie, *Adv Photonics Res*, 2021, 2, 2100066.
- xiii C. Yang, S. Wang, W. Chen, Y. Zhang, F. Guo, Y. Zhou, J. Wang and H. Han, *Chemistry – A European Journal*, 2023, 29, e202301677.
- xiv P. Kumar, T. D. Creason, H. Fattal, M. Sharma, M.-H. Du and B. Saporov, *Adv Funct Mater*, 2021, 31, 2104941.
- xv T. D. Creason, H. Fattal, I. W. Gilley, T. M. McWhorter, M.-H. Du and B. Saporov, *ACS Materials Au*, 2021, 1, 62–68.
- xvi K. Xu, L. Pérez-Fidalgo, B. L. Charles, M. T. Weller, M. I. Alonso and A. R. Goñi, *Sci Rep*, 2023, 13, 9300.
- xvii M. Coduri, T. B. Shiell, T. A. Strobel, A. Mahata, F. Cova, E. Mosconi, F. De Angelis and L. Malavasi, *Mater Adv*, 2020, 1, 2840–2845.
- xviii S. Sidhik, Y. Wang, M. De Siena, R. Asadpour, A. J. Torma, T. Terlier, K. Ho, W. Li, A. B. Puthirath, X. Shuai, A. Agrawal, B. Traore, M. Jones, R. Giridharagopal, P. M. Ajayan, J. Strzalka, D. S. Ginger, C. Katan, M. A. Alam, J. Even, M. G. Kanatzidis and A. D. Mohite, *Science*, 2022, 377, 1425–1430.
- xix V. Gutmann, *Coord Chem Rev*, 1976, 18, 225–255.
- xx J. C. Jr. Hamill, J. Schwartz and Y.-L. Loo, *ACS Energy Lett*, 2018, 3, 92–97.
- xxi N. Ahn, D.-Y. Son, I.-H. Jang, S. M. Kang, M. Choi and N.-G. Park, *J Am Chem Soc*, 2015, 137, 8696–8699.
- xxii T. D. Creason, A. Yangui, R. Roccanova, A. Strom, M.-H. Du and B. Saporov, *Adv Opt Mater*, 2020, 8, 1901338.
- xxiii S. Hull and P. Berastegui, *J Solid State Chem*, 2004, 177, 3156–3173.
- xxiv C. Hasselgren and S. Jagner, *Acta Crystallogr C*, 1999, 55, 1208–1210.
- xxv C. A. Schneider, W. S. Rasband and K. W. Eliceiri, *Nat Methods*, 2012, 9, 671–675.
- xxvi A. M. Ferraria, A. P. Carapeto and A. M. Botelho do Rego, *Vacuum*, 2012, 86, 1988–1991.
- xxvii Y. Tang, G. Pu, C. Kang, C. Li, X. Wang, M. Wang, H. Bi, W. Chen and J. Wang, *Mater. Horiz.*, 2024, 11, 6064–6072.
- xxviii Ibrahim, A. Shoukat, F. Aslam and M. Israr Ur Rehman, *Mol Phys*, 2024, 122(17), e2316273.
- xxix D. Banerjee and B. Saporov, *Chemistry of Materials*, 2023, 35, 3364–3385.
- xxx T. D. Creason, A. Yangui, R. Roccanova, A. Strom, M.-H. Du and B. Saporov, *Adv Opt Mater*, 2020, 8, 1901338.
- xxxi H. Xu, W. Liang, Z. Zhang, C. Cao, W. Yang, H. Zeng, Z. Lin, D. Zhao, G. Zou, *Adv. Mater.* 2023, 35, 2300136.
- xxxii G. Pu, R. Wang, Y. Tang, J. Song, J. Wang, *Mater. Chem. Front.*, 2025, 9, 1954–1970.
- xxxiii W. Gui, L. Yao, X. Zhou, C.-L. Wang, *J. Alloys Compd.*, 2025, 1014, 178667.
- xxxiv Y. Wang, S. Guo, H. Luo, C. Zhou, H. Lin, X. Ma, Q. Hu, M. Du, B. Ma, W. Yang and X. Lü, *J Am Chem Soc*, 2020, 142, 16001–16006.
- xxxv L. Han, H. Zhang, Y. Ning, H. Chen, C. Guo, J. Cui, G. Peng, Z. Ci and Z. Jin, *Chemical Engineering Journal*, 2022, 430, 132826.
- xxxvi K. Murata and S. Aoki, *Rev. High Press. Sci. Technol.*, 2016, 26, 3–7.
- xxxvii D. Staško, J. Prchal, M. Klicpera, S. Aoki and K. Murata, *High Press. Res.*, 2020, 40, 525–536.
- xxxviii J. D. Barnett, S. Block and G. J. Piermarini, *Rev. Sci. Instrum.*, 1973, 44, 1–9.
- xxxix W. B. Holzapfel, *J. Appl. Phys.*, 2003, 93, 1813–1818.
- xl CrysAlisPRO, Oxford Diffraction /Agilent Technologies UK Ltd., Yarnton, England.
- xli R. C. Clark and J. S. Reid, *Acta Cryst.*, 1995, A51, 887–897.
- xlii E. Spedicato, E. Bodon, A. D. Popolo, N. Mahdavi-Amiri, *4OR*, 2003, 1, 51–66.
- xliii G. M. Sheldrick, *Acta Cryst.*, 2015, A71, 3–8.



^{xliiv} O. V. Dolomanov, L. J. Bourhis, R. J. Gildea, J. A. K. Howard and H. Puschmann, *J. Appl. Cryst.*, 2009, 42, 339–341.

^{xliv} G. M. Sheldrick, *Acta Cryst.*, 2008, A64, 112–122.



Data Availability

View Article Online
DOI: 10.1039/D5TC03935E

The data supporting this article have been included as part of the Supplementary Information. Single crystal structure data in this work are available in the Inorganic Crystal Structure Database (ICSD), under deposition numbers CSD 2498636-2498649.

